A method for rapid estimation of residual stresses in metal samples produced by additive manufacturing

A. Fedorenko, D. Firsov, S. Evlashin
Center for Materials Technologies, Skolkovo Institute of Science and Technology, Russia
a.fedorenko@skoltech.ru, https://orcid.org/0000-0002-3260-7531
d.firsov@skoltech.ru, https://orcid.org/0000-0002-0640-9494
s.evlashin@skoltech.ru, https://orcid.org/0000-0001-6565-3748

B. Fedulov, E. Lomakin
Lomonosov Moscow State University, Russia
fedulov.b@mail.ru, https://orcid.org/0000-0002-1894-5964
evlomakin@yandex.ru, https://orcid.org/0000-0002-8716-5363

Citation: Fedorenko, A., Firsov, D., Evlashin, S., Fedulov, B., Lomakin, E., A method for rapid estimation of residual stresses in metal samples produced by additive manufacturing, Frattura ed Integrità Strutturale, 68 (2024) 267-279.

Received: 15.01.2024
Accepted: 20.02.2024
Published: 24.02.2024
Issue: 04.2024

KEYWORDS. Additive manufacturing, Residual stress, Stainless steel, Mechanics of materials, Mechanical properties.

INTRODUCTION

In additive manufacturing the ability to predict the resulting residual stresses stands as a critical factor influencing the quality, structural integrity, and lifespan of the produced part. The stresses developed during the process could lead to deformation or part failure, thus making their prediction and management of the utmost importance. Heat treatment

is a possible way to relieve residual stresses, but it also causes the reduction of exceptional properties in as-build conditions [1, 2]. Thus, various experimental and computational methods were adopted for the estimation of residual stresses.
The mechanical experimental methods are based on the analysis of part deflection due to the presence of residual stresses, and in the simplest applications are not require any expensive equipment. For example, Mercelis and Kruth [3] proposed a simple model for additive manufacturing of brick based on sequential adding of layers with the assumption of thermal shrinkage of every layer up to yield condition. A closed system of equations for forces and moments allows to calculate residual stresses before and after the separation with the use of part deflection after separation from the substrate. The demonstration of this modeling technique is also found in [4] for the photopolymerization process, in which the out-of-plane rotation of the additive polymer film is restricted during the process, and only in-plane stretching occurs. After separation from the substrate, the part will bend under its internal stress field.
More advanced mechanical methods, such as contour method [5], are based on the deformations measured on the entire surface of the produced part, so then residual stresses can be reconstructed [6].
The X-ray diffraction is a popular non-destructive method for residual stress measurements [7-9]. The major limitation of the method is a possibility of measurements only near the surface of the part. Therefore, a combination of different methods allows to understand better residual stress distribution both on surface and through the thickness of the part [10].
Neutron diffraction is the principal method of non-destructive measurement of residual stresses allowing to penetrate in the metals to many millimeters. The main drawback is the complexity and time consumption, since it requires the extraction of volumes at gage locations, which are considered as ones with stress-free lattice [11, 12]. Nevertheless, for the measurements at surface, neutron diffraction is accompanied by other methods [13].
For a review of other experimental techniques, readers are referred to [14, 15].
Many numerical methods for the computation of residual stresses rely on the solution of heat transfer problem coupled with thermo-mechanics [16-18]. These methods can be implemented using modern Finite Element Modeling (FEM) tools. However, the estimation of computational cost for direct analysis indicates that the mesh size should be of the order of micrometers (one-layer thickness), and the time increment is estimated to be on the nanosecond scale. To manage this unacceptable demand on computational resources, the mesh scaling approach is applied, where the thickness of one element corresponds to tens of physical layers of the deposited material. It also means, that local temperature extreme peaks are also neglected, as well as realistic elliptic shape of the laser profile is simplified as point heat source. Recent studies show that this approach can be used without a critical loss in accuracy [19, 20]. Further development of the concept for computational cost reduction is eigenstrain analysis [21], which provides a more approximate solution with less modeling and simulation time than thermal-stress analysis. It adopts a single stress analysis with predefined eigenstrains that represent the inelastic deformation induced by the processes, applied to each element upon activation. This method simplifies the problem definition by eliminating the need to specify detailed processing conditions.
In this study, we propose a simple method to estimate residual stress in steel cylindrical bars produced by laser powder bed fusion (LPBF). The basic idea involves making a partial longitudinal cut in the bar using electrical discharge machining (EDM) after its production. This procedure causes the double cantilever formed as a result to deviate from its original closed position. By measuring this deflection, we can apply equilibrium equations to assess the contribution of residual stresses to the equivalent bending moment. Although similar mechanical methods for analyzing residual stresses are well-established, our study introduces a distribution form for residual stress specifically for LPBF samples, supported by numerical analysis. This method allows estimate residual stresses in the laboratory without the need for special equipment. We consider a cylindrical shape since it is commonly used in mechanical testing, and understanding residual stresses in as-built conditions is crucial. Furthermore, while it is possible to extend the proposed method to other shapes, the axisymmetric geometry facilitates analysis and avoids the mathematical singularity found in the corners of rectangular bodies [22].

EXPERIMENTAL ANALYSIS

Samples preparation

The 316L stainless steel samples were produced using the 3D metal printer TruPrint 1000 (Trumpf) with the settings presented in previous studies [23]. The major parameters of the process are shown in Tab. 1. The powder of 316L stainless steel (Oerlikon, Freienbach, Switzerland) was used for the production of all specimens. The parts manufactured were assessed for relative porosity using an Axio Scope.A1 optical microscope (Carl Zeiss, Jena, Germany), following ASTM E1245 standard. The analysis revealed a porosity of not more than 0.1%.

LPBF Parameter	Value
Laser power	113 W
Laser spot diameter	55 μm
Hatch spacing	80 μm
Layer thickness	20 μm
Laser scan speed	700 mm/s
Gas speed (Ar)	2.5 m/s
Oxygen level	<0.3 at. %
Pressure in chamber	1 bar

Table 1: Process parameters for LPBF

Mechanical properties

Tensile stress-strain curves, obtained based on ISO 6892-1 standard for vertically-build samples, are presented in Fig. 1. The experiment was carried out on an Instron 5969 machine, operating at a quasi-static loading rate of 0.001 s^{-1}. Strain measurements were carried out utilizing the virtual extensometer method, implemented through a digital image correlation system (Correlated Solutions, Irmo, SC, USA). The measurements were based on a gauge length of 36 mm. It is notable that a moderate degree of anisotropy is typical for the LPBF steel [24-26]. In particular, some studies discuss a difference in elastic response depending on loading direction with the emphasis to Young's modulus reduction in vertical direction [27]. The nature of such difference is not fully understood, since different explanations found in literature and concern specific texture and residual stresses [28, 29]. In this study, following [30], we assume that the reduction of the Young's modulus in vertically-built samples is misrepresented due to the very high residual stresses. Therefore, the use of a Young's modulus of 196 GPa, obtained from testing horizontally-built samples with lower residual stresses, is more appropriate for LPBF simulation and aligns with the modulus of conventional steel. The stress-strain curves in the build direction, obtained experimentally in [30], are shown in Fig. 1. The properties used in modeling are summarized in Tab. 2.

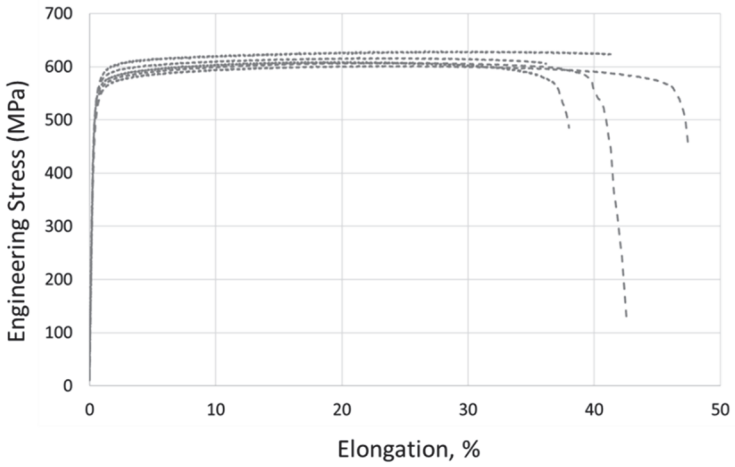

Figure 1: Tensile stress-strain curves.

Young's modulus, GPa	Yield stress, MPa	Ultimate stress, MPa	Elongation at break, %
196	528	612	39

Table 2: Tensile properties of LPBF 316L steel

Sample cutting experiment

As an experimental part of the method, we prepared four 80-mm long samples for each of three diameters: 6 mm, 8 mm, and 10 mm. After manufacturing, the samples were initially sectioned from the build plate, and subsequently, a wire EDM cut was performed from bottom to top according to the build position (Fig. 2). The cut was performed using an Accutom-100 machine equipped with a cooling water system. The length of the cut is 74 mm. The distance between the ends of the resulting cantilevers was measured. Therefore, the deflection is half of this distance, adjusted for the thickness of the material removed due to machining. The thickness of the material, removed by wire EDM, is approximately 0.4 mm.

Figure 2: Cylindrical samples of 6 mm, 8 mm and 10 mm after longitudinal cut.

NUMERICAL SIMULATION

General concept

A well-established approach for predicting residual stresses is based on thermomechanical simulations using the FEM. This approach is extensively presented in the literature for different methods of metal processing, such as welding [31, 32] and shock peening [33]. A model for the LPBF process involves solving heat transfer problems for elements that are sequentially activated according to the part-building strategy, under conditions of laser scanning, heat convection, and re-radiation. The mechanical analysis involves simulating the thermal expansion and shrinkage of the activated elements following the temperature history. While some studies have aimed to capture microstructural features [34], the commonly FEM-based approach typically neglects many aspects of the LPBF process such as phase transformations, melt pool, and microstructural evolution. Additionally, it is impossible to represent every layer deposition since meshing on such small scale leads to an unacceptable computational cost. For this reason, a dump-block approach is commonly used, in which one element corresponds to tens of physical layers [35, 36]. A detailed analysis of this simplification and the influence of different parameters is discussed in [20].

Using the dump-block approach for a part of simple geometry, such as a cylindrical bar, it is also possible to avoid a direct simulation of thermal conductivity during part manufacturing. Indeed, the local peak temperature after laser spot passage drops rapidly up to some temperature T_f by the moment of powder deposition for the next layer. Following this idea, we can assume that every layer is activated at some activation temperature T_{sf} and cools down up to T_f, inducing residual stress due to the shrinkage. The final temperature T_f can be measured during the part build process, or simply assumed to be uniform and equal to the temperature of the build plate. The temperature T_{sf} has no clear physical meaning, but it strongly affects the solution and can be calibrated experimentally. The described assumptions are also similar to the eigenstrains concept, in which blocks of elements are activated with some predefined strains.

For the modeling of part production, following [30] we assume that at every step of the analysis, the entire 0.4 mm - thick layer appears at activation temperature T_{sf}=800 °C and cools down up to the build plate temperature T_f=80 °C. The analysis was performed using Abaqus commercial software [37]. The mesh is represented by solid C3D8R elements with an average side length of 0.4 mm, with the number of elements varies from 44,000 for the bar of diameter 6 mm to 127,000 elements for the 10 mm diameter. In the model, the bottommost layer of vertically-oriented bar has fixed boundary conditions to simulate adjustment to the build plate. Upon completion of the build process simulation, we proceed to model the separation of the part from the build plate. This model first involves the removal of the bottom layer of elements, followed by the removal of a thin layer of elements along the diameter, in accordance with the experimental procedure for cutting in the longitudinal direction.

As the boundary conditions were originally set on the bottom elements, which are then suggested for removal, we change the fixed condition to the opposite end of the sample. Consequently, the resulting structure can be viewed as a cantilever. Next, a partial longitudinal cut is performed from the free end of the cantilever, causing the newly obtained double cantilever to deviate from its closed position. This cut was performed from bottom to top of the sample. The removal of elements corresponds to assigning them zero stiffness and yield stress; thus, the resulting 'dead' elements do not transfer any load. The model does not account for damage. Despite the procedure's dependency on the sequence of element removal, it does not introduce significant errors to the stresses noticeably far from the cutting zone.

Constitutive behavior

A complete, closed-form set of governing equations intended for numerical implementation in FEA algorithms is cumbersome. It has been presented in many studies, for example, [19, 20]. However, the subsequent equations give the understanding of constitutive modeling:

$$\varepsilon_{th} = \alpha(T)\Delta T \tag{1, a}$$

$$\varepsilon = \varepsilon_{el} + \varepsilon_{pl} + \varepsilon_{th} \tag{1, b}$$

$$\sigma = C(T) : \varepsilon_{el} \tag{1, c}$$

$$f_{yield} = \sqrt{\frac{2}{3} S_{ij} S_{ij}} - \sigma_0(\varepsilon_{eq},\ T) \tag{1, d}$$

where $\alpha(T)$ is a thermal expansion coefficient, the total strain tensor ε is a sum of elastic (ε_{el}), plastic (ε_{pl}) and thermal (ε_{th}) strains, $C(T)$ is temperature-dependent elastic stiffness tensor, S_{ij} is a stress deviator, and $\sigma_0(\varepsilon_{eq},\ T)$ defines temperature-dependent yield conditions, ε_{eq} is equivalent plastic strain. A classic plasticity with isotropic hardening is used. The temperature-dependent plasticity behavior of the material is desirable to take into account to increase the accuracy. Due to limitations in temperature-dependent test data, a common approach to implement this is by scaling hardening curves according to temperature [12]. However, the secondary-order importance of temperature-dependent behavior is reported in [38]. Moreover, even the selection of temperature-dependent hardening curves requires calibration to fit experimental data, as demonstrated in [20]. In summary, hardening under normal thermal conditions is used, as it is calibrated by selecting T_{sf} to induce part deflection that aligns with experimental results.

LPBF simulation results

The residual stress distribution in prismatic parts in as-built conditions has been discussed in several experimental studies [10, 12, 39]. These studies concluded that the interior is under high compressive stress, balanced by tensile stress near the outer surface. Furthermore, the stress level is considered to be close to yield conditions. To illustrate this result, the axisymmetric distribution of σ_z (along the cylinder), obtained by the numerical modeling described in the previous section, is shown for a 10-mm diameter bar in Fig. 3 (a). The deflection of two cantilevers after the final cut with respect to the build direction and boundary conditions is shown in Fig. 3 (b). This represents the final state of the structure, which is in equilibrium with the residual stresses after all stages of modeling. It should be noted that fixed top surface is far from the cut tip and doesn't affect the deflection. For the analytical method proposed in this study, it is also important to understand the effect of plastic deformations after the cut. As shown in Fig. 3 (c), the equivalent plastic strain for the entire process (build and cut) does not exceed 3%, which leads us to assume that yield does not occur during cutting.

The stress components in cylindrical coordinates $\sigma_z = (\sigma_r,\ \sigma_\vartheta,\ \sigma_z)$, $p = -1/3(\sigma_r + \sigma_\vartheta + \sigma_z)$ and equivalent von Mises stress σ_0 along the 5-mm long radius are presented in Fig. 4. From the plots one can observe, that the absolute value of σ_z in the center of the bar is excess σ_0 due to the effect of hydrostatic stress. In other words, σ_z above the yield stress are possible within the assumptions of the present model.

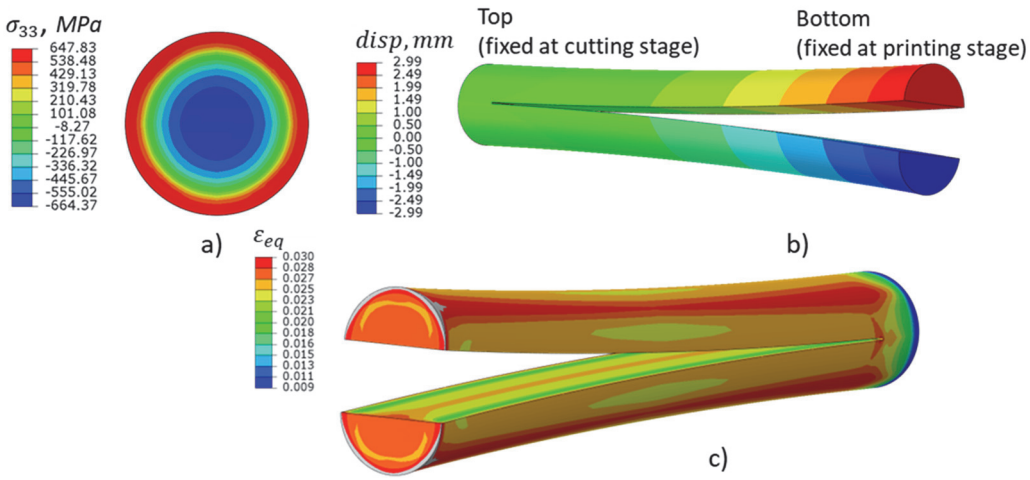

Figure 3: (a) Cross-section displaying axial stress in a 5 mm radius bar prior to the cut, (b) deflection of the double cantilever after cut, and (c) equivalent plastic strain after cut.

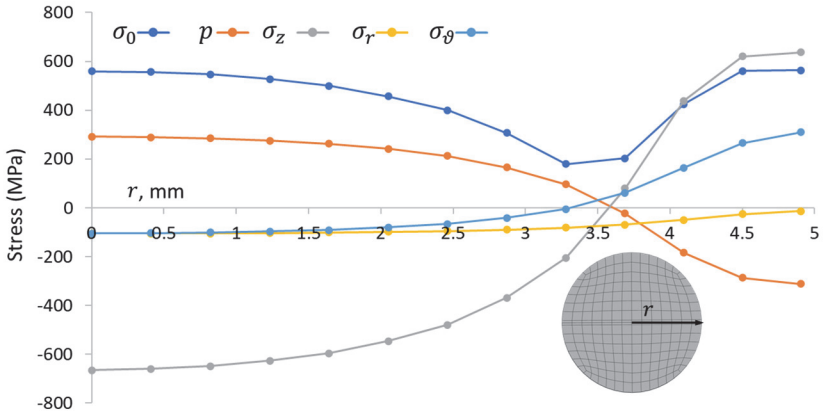

Figure 4: Stress characteristics along the 5-mm radius of the bar.

Comparison of FEM-predicted deflection with experiment

The distance between the halves of the bar after cut (measured as average distance between corners of the obtained cantilevers) is presented in Tab. 3 and compared with predicted value using the model. In the model the nodes for distance measurements are taken at the distance 0.2 mm from the cutting plane (so initially they located at 0.4 mm from each other, what corresponds to the thickness of removed material).

	Max. distance between halves of the bar after cut, mm		
	D=6 mm	D=8 mm	D=10 mm
Test #1	10.65	7.63	5.84
Test #2	10.67	7.50	6.03
Test #3	9.98	7.58	6.19
Test #4	10.25	7.20	6.14
Mean	10.39	7.48	6.17
Prediction	10.61	8.10	5.97

Table 3: Comparison of experimentally measured deflections with model prediction for the bars of different diameters.

CALCULATIONS BASED ON CANTILEVER DEFLECTION

In the proposed method, we find the distribution of the axial component of residual stress σ_z (σ_z is also referred as the normal stress in cross-section). It is assumed that the stress distribution is the same for all cross-sections along the bar axis. The form of dependency for σ_z on the cylinder's radius *r*, prior to cutting, can be postulated parametrically based on stresses obtained in the numerical simulation. After longitudinally cutting the bar, the halves deflect and we treat each half as a cantilever beam under pure bending conditions, with an equivalent moment *M* at the support. The moment *M* can be found assuming pure bending with simplifications of the classical Euler-Bernoulli beam theory. an equation of deflected beam after cut reads as follows:

$$M = \frac{2\delta E J_S}{L^2} \tag{2}$$

where δ is a deflection of one cantilever, E is Young's modulus, J_S is a second moment of inertia with respect to neutral axis where $\sigma_z = 0$, and L is a length of the beam (is equal to the length of the cut).

The only unknown parameter in (2) is a J_S. To determine it, note that the cross-section of the cantilever is not an exact half-circle due to the additional extraction of a material layer of thickness h during the EDM process, as shown in Fig. 5. Similarly, the deflection δ for the (2) is selected as a half of mean value from Tab. 3, corrected to the -h/2 term.

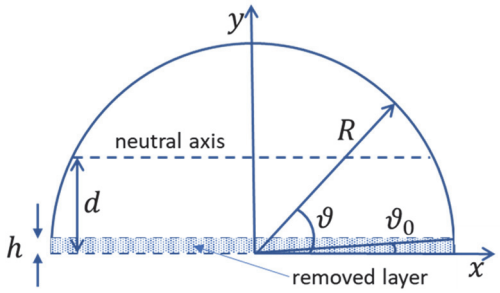

Figure 5: Notations for calculation over half circle.

Using the notations for the cross-section in Fig. 5, the neutral axis location at distance d can be found from the equation on first moment of inertia:

$$J_f = 2\int_h^R (y - d)\left(R^2 - y^2\right)^{1/2} dy = 0 \tag{3}$$

The second moment of inertia can be calculated using the following formula, once d is obtained from the Eqn. (3):

$$J_S = 2\int_h^R (y - d)^2 \left(R^2 - y^2\right)^{1/2} dy \tag{4}$$

On the other hand, the equilibrium equations for forces and moment are valid for the half of the bar before the cut:

$$\iint_S \sigma_z = 0, \tag{5, a}$$

$$\iint_{S_1} y \cdot \sigma_z = M, \tag{5, b}$$

where the axial stress σ_z is integrated over an exact half-circle S for the force equation, and over the reduced area S_1 to the h-height slice to match bending moment *M*, since it is calculated based on the reduced part. In this study due to the axial symmetry of the problem, so σ_z depends only on radius: $\sigma_z = \sigma_z(r)$.
It is convenient to rewrite Eqns. (5) in cylindrical coordinates as follows:

$$\int_0^{\pi}\int_0^{R} \sigma_z(r)\cdot r dr d\vartheta = 0, \tag{6, a}$$

$$\int_{\vartheta_0}^{\pi-\vartheta_0}\int_{h/\sin\vartheta}^{R} \sigma_z(r)\cdot(r\sin\vartheta - d) dr d\vartheta = M, \tag{6, b}$$

so that integration limits in (6, b) allow to extract the contribution from the removed slice according to Fig. 5.
Now the following trial forms for the stress distribution can be considered:

$$\sigma_z(r) = ar + b; \tag{7, a}$$

$$\sigma_z(r) = ar^2 + b; \tag{7, b}$$

$$\sigma_z(r) = -\sigma_0 \text{ for } r \le R_0,\ \sigma_z(r) = ar + b \text{ for } R_0 \le r \le R; \tag{7, c}$$

$$\sigma_z(r) = -\sigma_0 \text{ for } r \le R_0,\ \sigma_z(r) = ar + b \text{ for } R_0 \le r \le R_1,\ \sigma_z(r) = \sigma_0 \text{ for } R_1 \le r \le R. \tag{7, d}$$

The first two relations (6, a) and (6, b) implement assumption of linear and parabolic approximation of stress variation along the radius without considering plasticity. The relations (6, c) and (6, d) take into account the presence of plastic conditions. However, for the relation (6, c) it is assumed, that yielding occurs only in central region. Therefore, $\sigma_z(r) = -\sigma_0$ holds up to a certain radius R_0, and beyond it, the linear relation is satisfied. For the last assumption (6, d), the compressive yield condition $\sigma_z(r) = -\sigma_0$ occurs in the central region $r \le R_0$. In contrast, in the outer region where $R_0 \le r \le R$, the plastic criterion on tension $\sigma_z(r) = \sigma_0$ holds (equal tensile and compressive yield stress is assumed). For plasticity consideration, we also assume perfect plasticity with $\sigma_0 = 600$ MPa, corresponding approximately to the plateau stress in Fig. 1. The transition region between zones of plasticity is constructed linearly.
With the proposed forms for stress dependency, one can substitute them and solve Eqn. (6) to find two unknown parameters. Indeed, since only two equilibrium equations were formulated, two-parametric forms for $\sigma_z(r)$ were proposed. However, the number of parameters can be increased at the expense of additional experimental data. For instance, one can consider additional tests for beam bending [40], or some technique for measuring on-surface residual stress.

DISCUSSION

By substituting the mean experimental deflections of samples with diameters D=6 mm, D=8 mm and D=10 mm into Eqn. (2), one can calculate the equivalent bending moment *M* in every case. Note once again that δ is half of the mean value presented in Tab. 3, minus half thickness of the machined slice. With *M* known, Eqns. 6 are solved to find a relation for $\sigma_z(r)$ in each sample. In Figs. 6-8, we compare the calculated $\sigma_z(r)$ along the radius using the proposed method with residual stress distribution obtained by the FE analysis.
The linear assumption (7, a) gives an unacceptable $\sigma_z(r)$ prediction near the center for all diameters but predicts well at the outer radius for samples of all diameters. The parabolic relation (7, b) still overestimates value at the center and the agreement with the FEM prediction is much better. Both relations (7, a) and (7, b) have a shortcoming due to their neglect of plasticity, while yield stress is observed in the simulation.

The relations (7, c) and (7, d), where plasticity is considered, are referred as one-side and two-side plastic, following to the number of end "caps" with the plastic zones. A significant difference between (7, c) and (7, d) is observed for the samples with D=6 mm and D=8 mm, while for D=10 mm the calculated stress is rather similar. The agreement of (7, d) with the FEM underscores the importance of considering plasticity for the cases with high residual stresses. As can be observed, the two-sided plastic assumptions of (7, d) provide the best fit for the reference result.

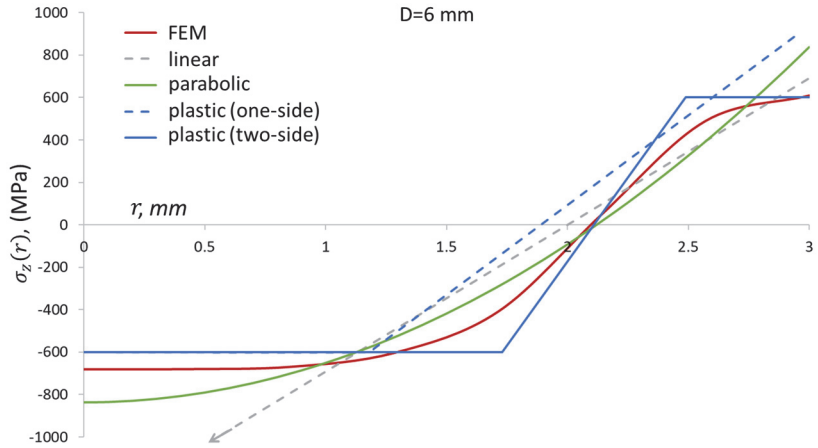

Figure 6: Application of relations (7) for $\sigma_z(r)$ prediction in samples of 6 mm diameter: comparison with FEM-based prediction.

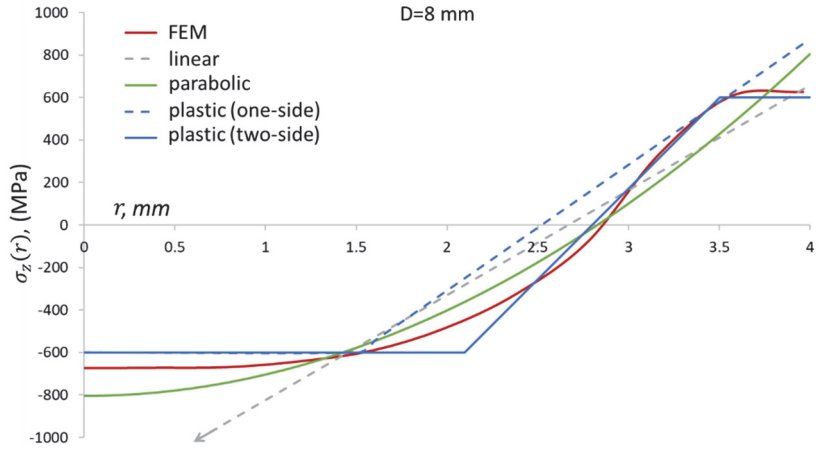

Figure 7: Application of relations (7) for $\sigma_z(r)$ prediction in samples of 8 mm diameter: comparison with FEM-based prediction.

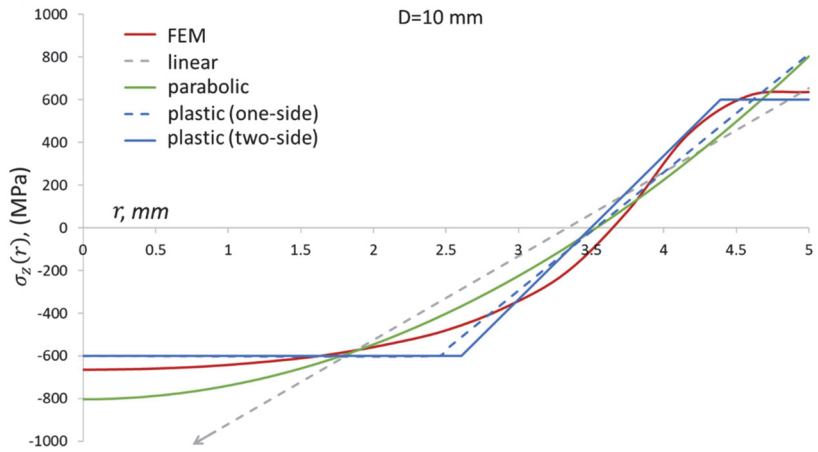

Figure 8: Application of relations (7) for $\sigma_z(r)$ prediction in samples of 10 mm diameter: comparison with FEM-based prediction.

While (7, a) and (7, b) give overestimation of $\sigma_z(r)$ in the presented cases, they might be beneficial to use it for samples with lower residual stresses. For instance, neglecting the thickness of removed layer h, it is possible to represent J_s for (2) as follows:

$$J_S = \frac{R^4\left(9\pi^2 - 64\right)}{72\pi} \tag{8}$$

Now it is possible to solve Eqn. (6) and find $\{a,\ \mathrm{b}\}$ pair in explicit form:

$$\left\{a = \frac{E\cdot\delta\cdot\left(9\pi^2-64\right)}{2\pi L^2},\ \mathrm{b} = -\frac{E\cdot\delta\cdot\left(9\pi^2-64\right)}{3\pi L^2}\right\} \text{ for (7, a)} \tag{9, a}$$

$$\left\{a = \frac{5E\cdot\delta\cdot\left(9\pi^2-64\right)}{12\pi L^2},\ \mathrm{b} = -\frac{5E\cdot\delta\cdot\left(9\pi^2-64\right)}{24\pi L^2}\right\} \text{ for (7, b)} \tag{9, b}$$

Using formulae (9), one can instantly obtain the residual stress distribution assuming a linear and quadratic distribution. For practical applications, once the experiment is performed, the expression (9, b) is recommended as first choice, due to the more realistic stress distribution, consistent with experimental studies. If the result exceeds the yield limit, an analysis based on the assumption of perfect plasticity can be used. Indeed, understanding high residual stresses close to yield stress is useful in itself and helps in making decisions about heat treatment or changing the build strategy. The subsequent consideration with the presence of plasticity allows for better understanding of potential stress distribution configurations.

For the limits of the plastic caps, an approximate value of σ_0=600 MPa was applied, so the analysis of the sensitivity to σ_0 is demonstrated in Fig. 9 considering different diameters. As can be seen, a variation of σ_0 between 560-700 MPa leads to a significant change in the stress transition zone between compression and tension. Furthermore, a decrease in σ_0 leads to an incompatible stress distribution since intermediate line tends to a vertical one. Specifically, the solution for (7, d) does not exist for the case of diameter D=6 mm with σ_0=560 MPa. In contrast, if we increase σ_0, the solution tends to one-side plastic zone (7, c).

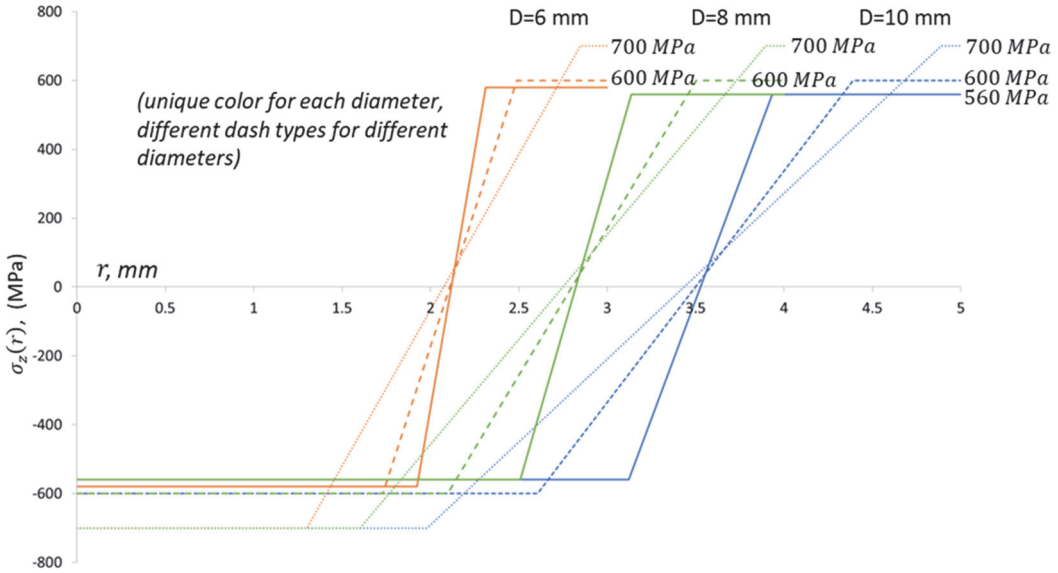

Figure 9: Influence of yield stress σ_0 on $\sigma_z(r)$ using the assumptions of two-side plasticity for stress distribution within samples of different diameters. A unique color is selected for each diameter.

CONCLUSIONS

This paper proposes an effective method for estimation of residual stress in 316L stainless steel LPBF cylindrical samples without using specific equipment. The experimental component involves preparing a cut along the bar and measuring the cantilever deviations. We consider only the form for the axial stress component $\sigma_z(r)$ as it plays a dominant role compared to other stress components. The method is verified using FEM as a reference for residual stress distribution within bars of diameters 6 mm, 8 mm, and 10 mm in as-built conditions. Results calculated using the proposed method align well with FEM, if plastic conditions are included in the assumed relation for $\sigma_z(r)$. However, linear and parabolic forms for $\sigma_z(r)$ are useful for the cases with moderate residual stresses or for examining if yield occurs. The method's accuracy can be enhanced with additional experimental data, which would allow for the examination of dependency driven by more than two parameters. For example, it is possible to measure the residual stress on the outer surface using X-ray diffraction, which provides a known point for stress approximation.

ACKNOWLEDGEMENTS

This work was supported by the Russian Science Foundation, grant No. 20-11-20230-P.

REFERENCES

[1] Ronneberg, T., Davies, C.M., Hooper, P.A. (2020). Revealing relationships between porosity, microstructure and mechanical properties of laser powder bed fusion 316L stainless steel through heat treatment, Mater Des, 189, p. 108481. DOI: 10.1016/j.matdes.2020.108481.

[2] Yin, Y.J., Sun, J.Q., Guo, J., Kan, X.F., Yang, D.C. (2019). Mechanism of high yield strength and yield ratio of 316 L stainless steel by additive manufacturing, Materials Science and Engineering A, 744(December 2018), pp. 773–777. DOI: 10.1016/j.msea.2018.12.092.

[3] Mercelis, P., Kruth, J.P. (2006). Residual stresses in selective laser sintering and selective laser melting, Rapid Prototyp J, 12(5), pp. 254–265. DOI: 10.1108/13552540610707013.

[4] Zhao, Z., Wu, J., Mu, X., Chen, H., Qi, H.J., Fang, D. (2017). Origami by frontal photopolymerization, Sci Adv, 3(4). DOI: 10.1126/sciadv.1602326.

[5] Prime, M.B. (2001). Cross-Sectional Mapping of Residual Stresses by Measuring the Surface Contour After a Cut, J Eng Mater Technol, 123(2), pp. 162–168. DOI: 10.1115/1.1345526.

[6] Uzun, F., Korsunsky, A.M. (2023). Voxel-Based Full-Field Eigenstrain Reconstruction of Residual Stresses, Adv Eng Mater, 25(14). DOI: 10.1002/adem.202201502.

[7] Liu, Y., Yang, Y., Wang, D. (2016). A study on the residual stress during selective laser melting (SLM) of metallic powder, International Journal of Advanced Manufacturing Technology, 87(1–4), pp. 647–656. DOI: 10.1007/s00170-016-8466-y.

[8] Serrano-Munoz, I., Fritsch, T., Mishurova, T., Trofimov, A., Apel, D., Ulbricht, A., Kromm, A., Hesse, R., Evans, A., Bruno, G. (2021). On the interplay of microstructure and residual stress in LPBF IN718, J Mater Sci, 56(9), pp. 5845–5867. DOI: 10.1007/s10853-020-05553-y.

[9] Song, X., Xie, M., Hofmann, F., Illston, T., Connolley, T., Reinhard, C., Atwood, R.C., Connor, L., Drakopoulos, M., Frampton, L., Korsunsky, A.M. (2015). Residual stresses and microstructure in Powder Bed Direct Laser Deposition (PB DLD) samples, International Journal of Material Forming, 8(2), pp. 245–254. DOI: 10.1007/s12289-014-1163-1.

[10] Rangaswamy, P., Griffith, M.L., Prime, M.B., Holden, T.M., Rogge, R.B., Edwards, J.M., Sebring, R.J. (2005). Residual stresses in LENS® components using neutron diffraction and contour method, Materials Science and Engineering A, 399(1–2), pp. 72–83. DOI: 10.1016/j.msea.2005.02.019.

[11] Charmi, A., Falkenberg, R., Ávila, L., Mohr, G., Sommer, K., Ulbricht, A., Sprengel, M., Saliwan Neumann, R., Skrotzki, B., Evans, A. (2021). Mechanical anisotropy of additively manufactured stainless steel 316L: An experimental and numerical study, Materials Science and Engineering A, 799, p. 140154. DOI: 10.1016/j.msea.2020.140154.

[12] Williams, R.J., Vecchiato, F., Kelleher, J., Wenman, M.R., Hooper, P.A., Davies, C.M. (2020). Effects of heat treatment on residual stresses in the laser powder bed fusion of 316L stainless steel: Finite element predictions and neutron diffraction measurements, J Manuf Process, 57, pp. 641–653. DOI: 10.1016/j.jmapro.2020.07.023.
[13] Wu, A.S., Brown, D.W., Kumar, M., Gallegos, G.F., King, W.E. (2014). An Experimental Investigation into Additive Manufacturing-Induced Residual Stresses in 316L Stainless Steel, Metall Mater Trans A Phys Metall Mater Sci, 45(13), pp. 6260–6270. DOI: 10.1007/s11661-014-2549-x.
[14] Withers, P.J., Bhadeshia, H.K.D.H. (2001). Residual stress part 1 - Measurement techniques, Materials Science and Technology, 17(4), pp. 355–365. DOI: 10.1179/026708301101509980.
[15] Acevedo, R.B.O., Kantarowska, K., Santos, E.C., Fredel, M.C. (2020). Residual stress measurement techniques for Ti6Al4V parts fabricated using selective laser melting: state of the art review, Rapid Prototyp J. DOI: 10.1108/RPJ-04-2019-0097.
[16] Bugatti, M., Semeraro, Q. (2018). Limitations of the inherent strain method in simulating powder bed fusion processes, Addit Manuf, 23(June), pp. 329–346. DOI: 10.1016/j.addma.2018.05.041.
[17] Mukherjee, T., Zhang, W., DebRoy, T. (2017). An improved prediction of residual stresses and distortion in additive manufacturing, Comput Mater Sci, 126, pp. 360–372. DOI: 10.1016/j.commatsci.2016.10.003.
[18] Dunbar, A.J., Denlinger, E.R., Gouge, M.F., Michaleris, P. (2016). Experimental validation of finite element modeling for laser powder bed fusion deformation, Addit Manuf, 12, pp. 108–120. DOI: 10.1016/j.addma.2016.08.003.
[19] Song, X., Feih, S., Zhai, W., Sun, C.N., Li, F., Maiti, R., Wei, J., Yang, Y., Oancea, V., Romano Brandt, L., Korsunsky, A.M. (2020). Advances in additive manufacturing process simulation: Residual stresses and distortion predictions in complex metallic components, Mater Des, 193, p. 108779. DOI: 10.1016/j.matdes.2020.108779.
[20] Singh, U.P., Swaminathan, S., Phanikumar, G. (2022). Thermo-mechanical approach to study the residual stress evolution in part-scale component during laser additive manufacturing of alloy 718, Mater Des, 222, p. 111048. DOI: 10.1016/j.matdes.2022.111048.
[21] Salvati, E., Korsunsky, A.M. (2018). A simplified FEM eigenstrain residual stress reconstruction for surface treatments in arbitrary 3D geometries, Int J Mech Sci, 138–139, pp. 457–466. DOI: 10.1016/j.ijmecsci.2018.02.016.
[22] Fedulov, B.N., Bondarchuk, D.A., Fedorenko, A.N., Lomakin, E. V. (2022). Residual stresses near the free edge of composite materials, Acta Mech, 233(2), pp. 417–435. DOI: 10.1007/s00707-021-03113-2.
[23] Filimonov, A.M., Rogozin, O.A., Firsov, D.G., Kuzminova, Y.O., Sergeev, S.N., Zhilyaev, A.P., Lerner, M.I., Toropkov, N.E., Simonov, A.P., Binkov, I.I., Okulov, I. V., Akhatov, I.S., Evlashin, S.A. (2020). Hardening of Additive Manufactured 316L Stainless Steel by Using Bimodal Powder Containing Nanoscale Fraction, Materials, 14(1), p. 115. DOI: 10.3390/ma14010115.
[24] Mooney, B., Kourousis, K.I., Raghavendra, R. (2019). Plastic anisotropy of additively manufactured maraging steel: Influence of the build orientation and heat treatments, Addit Manuf, 25(September 2018), pp. 19–31. DOI: 10.1016/j.addma.2018.10.032.
[25] Shamsujjoha, M., Agnew, S.R., Fitz-Gerald, J.M., Moore, W.R., Newman, T.A. (2018). High Strength and Ductility of Additively Manufactured 316L Stainless Steel Explained, Metall Mater Trans A Phys Metall Mater Sci, 49(7), pp. 3011–3027. DOI: 10.1007/s11661-018-4607-2.
[26] Güden, M., Yavaş, H., Tanrıkulu, A.A., Taşdemirci, A., Akın, B., Enser, S., Karakuş, A., Hamat, B.A. (2021). Orientation dependent tensile properties of a selective-laser-melt 316L stainless steel, Materials Science and Engineering A, 824(June). DOI: 10.1016/j.msea.2021.141808.
[27] Im, Y.D., Kim, K.H., Jung, K.H., Lee, Y.K., Song, K.H. (2019). Anisotropic Mechanical Behavior of Additive Manufactured AISI 316L Steel, Metall Mater Trans A Phys Metall Mater Sci, 50(4), pp. 2014–2021. DOI: 10.1007/s11661-019-05139-7.
[28] Wang, Z., Jiang, B., Wu, S., Liu, W. (2023). Anisotropic tension-compression asymmetry in SLM 316L stainless steel, Int J Mech Sci, 246, p. 108139. DOI: 10.1016/j.ijmecsci.2023.108139.
[29] Zinovieva, O., Romanova, V., Zinoviev, A., Nekhorosheva, O., Balokhonov, R. (2023). Elastic properties of additively manufactured steel produced with different scan strategies, Int J Mech Sci, 244. DOI: 10.1016/j.ijmecsci.2022.108089.
[30] Fedorenko, A., Fedulov, B., Kuzminova, Y., Evlashin, S., Staroverov, O., Tretyakov, M., Lomakin, E., Akhatov, I. (2021). Anisotropy of mechanical properties and residual stress in additively manufactured 316l specimens, Materials, 14(23), pp. 1–17. DOI: 10.3390/ma14237176.
[31] Ferro, P., Bonollo, F., Berto, F., Montanari, A. (2019). Numerical modelling of residual stress redistribution induced by TIG-dressing, Frattura Ed Integrita Strutturale, 13(47), pp. 221–230. DOI: 10.3221/IGF-ESIS.47.17.
[32] Szávai, S., Bezi, Z., Ohms, C. (2016). Numerical simulation of dissimilar metal welding and its verification for determination of residual stresses, Frattura Ed Integrita Strutturale, 10(36), pp. 36–45. DOI: 10.3221/IGF-ESIS.36.04.

[33] Kostina, A., Zhelnin, M., Gachegova, E., Prokhorov, A., Vshivkov, A., Plekhov, O., Swaroop, S. (2022). Finite-element study of residual stress distribution in Ti-6Al-4V alloy treated by laser shock peening with varying parameters, Frattura Ed Integrita Strutturale, 16(61), pp. 419–436. DOI: 10.3221/IGF-ESIS.61.28.

[34] Zhang, Q., Xie, J., Gao, Z., London, T., Griffiths, D., Oancea, V. (2019). A metallurgical phase transformation framework applied to SLM additive manufacturing processes, Mater Des, 166. DOI: 10.1016/j.matdes.2019.107618.

[35] Williams, R.J., Davies, C.M., Hooper, P.A. (2018). A pragmatic part scale model for residual stress and distortion prediction in powder bed fusion, Addit Manuf, 22(May), pp. 416–425. DOI: 10.1016/j.addma.2018.05.038.

[36] Pant, P., Sjöström, S., Simonsson, K., Moverare, J., Proper, S., Hosseini, S., Luzin, V., Peng, R. (2021). A Simplified Layer-by-Layer Model for Prediction of Residual Stress Distribution in Additively Manufactured Parts, Metals (Basel), 11(6), p. 861. DOI: 10.3390/met11060861.

[37] Abaqus User's Manual, https://help.3ds.com/2021/

[38] Yang, Y., Allen, M., London, T., Oancea, V. (2019). Residual Strain Predictions for a Powder Bed Fusion Inconel 625 Single Cantilever Part, Integr Mater Manuf Innov, 8(3), pp. 294–304. DOI: 10.1007/s40192-019-00144-5.

[39] Sprengel, M., Mohr, G., Altenburg, S.J., Evans, A., Serrano-Munoz, I., Kromm, A., Pirling, T., Bruno, G., Kannengiesser, T. (2022). Triaxial Residual Stress in Laser Powder Bed Fused 316L: Effects of Interlayer Time and Scanning Velocity, Adv Eng Mater, 24(6). DOI: 10.1002/adem.202101330.

[40] Korsunsky, A.M., Withers, P.J. (1997). Plastic bending of a residually stressed beam, Int J Solids Struct, 34(16), pp. 1985–2002. DOI: 10.1016/S0020-7683(96)00141-2.